Composites: Part A 172 (2023) 107587

Contents lists available at ScienceDirect

Composites Part A

journal homepage: www.elsevier.com/locate/compositesa

Carbon Fiber-Reinforced Piezoelectric Nanocomposites: Design, Fabrication and Evaluation for Damage Detection and Energy Harvesting

Yaonan Yu [a], Yu Shi [b,*], Hiroki Kurita [a], Yu Jia [c], Zhenjin Wang [a], Fumio Narita [a,*]

[a] Department of Frontier Sciences for Advanced Environment, Graduate School of Environmental Studies, Tohoku University, Sendai, Japan
[b] Department of Physical, Mathematical and Engineering Sciences, University of Chester, Pool Lane, Chester, UK
[c] School of Engineering and Applied Science, Aston University, Birmingham, UK

ARTICLE INFO

Keywords:
Piezoelectricity
Carbon Fiber-Reinforced Polymers Electrode
End-Notched Flexure
Damage Detection

ABSTRACT

Carbon fiber-reinforced polymers (CFRPs) can be used in aging infrastructures as a reinforcement because of their excellent mechanical properties, and they can also be used in the support maintenance and repair work of these structures. However, the development of CFRPs as reinforcement while achieving self-powered damage detection is still challenging. Herein, a sodium potassium niobate (KNN) nanoparticle-filled epoxy (KNN–EP) plate was fabricated and combined with advanced CFRP electrodes. The obtained composites exhibited dramatically enhanced mechanical properties. In addition, CFRP contributed to the energy harvesting output (peak-to-peak output voltage V_{pp} = 7.25 mV), which was over 600 % higher than that of the KNN–EP plate. Thus, this composite could work as a force sensor for damage detection. In the end-notch bending test, the voltage signals generated by CFRP/KNN–EP composite accurately corresponded to the crack growth, which could provide the real-time crack state and prediction of fracture occurrence. Therefore, this work provided a new strategy for structural enhancement and kinetic energy harvesting, which can be used to detect damage behavior in infrastructures.

1. Introduction

Infrastructure safety against accidents, such as structural failures caused by structure deterioration and hazardous events, can cause significant economic and life losses and pose a great threat to the well-being of society. Thus, it has long been a top priority for governmental agencies. Carbon fiber-reinforced polymers (CFRPs) are mainly composed of carbon fiber and matrix materials, making them lightweight materials with high strength and modulus [1–3]. In recent years, CFRPs have been widely used to reinforce and maintain aging infrastructures [4–6]. Compared to maintenance work, achieving structural enhancement while maintaining accurate and timely structural health monitoring (SHM) of aging infrastructures remains a challenge. SHM is an assessment process of the in-service health of a structure to enhance the maintenance efficiency using a sensing system [7]. Structural damage detection methods, such as acoustic emission [8–10], computer vision [11,12], and visual inspection [13], have been widely used. However, these methods usually require complex external devices to perform the sensing and signal output functions. Alsaadi et al. [14] reported a method using the piezoresistive properties of carbon fibers to detect the damage in CFRP materials due to low-velocity impact events. The study demonstrated that high-performance composites with self-sensing properties are promising detection materials. Nevertheless, self-powered structures are still under investigation. Structurally self-powered refers to the ability of a structural material to act as a power source to eliminate the need for embedded or attached power sources. With the rapid development of the Internet of Things (IoT), the research of lead-free piezoelectric materials applied in self-powered sensors has been widely studied [15–17].

Piezoelectric materials have emerged as promising candidates for various industrial and scientific applications owing to their unique electromechanical properties [18]. These materials can generate electric charge when subjected to mechanical stress. Furthermore, they can deform in response to an applied electric field [19]. A piezoelectric material is an attractive choice for multifunctional composites that can serve as a structural material and a sensing system [20,21].

Incorporating piezoelectric material into fiber-reinforced composites provides a material that has the strength and stiffness of conventional

* Corresponding authors.
E-mail addresses: yu.yaonan.p5@dc.tohoku.ac.jp (Y. Yu), y.shi@chester.ac.uk (Y. Shi), kurita@tohoku.ac.jp (H. Kurita), y.jia1@aston.ac.uk (Y. Jia), zhenjin.wang.d6@tohoku.ac.jp (Z. Wang), narita@material.tohoku.ac.jp (F. Narita).

https://doi.org/10.1016/j.compositesa.2023.107587
Received 24 January 2023; Received in revised form 1 April 2023; Accepted 17 April 2023
Available online 22 April 2023

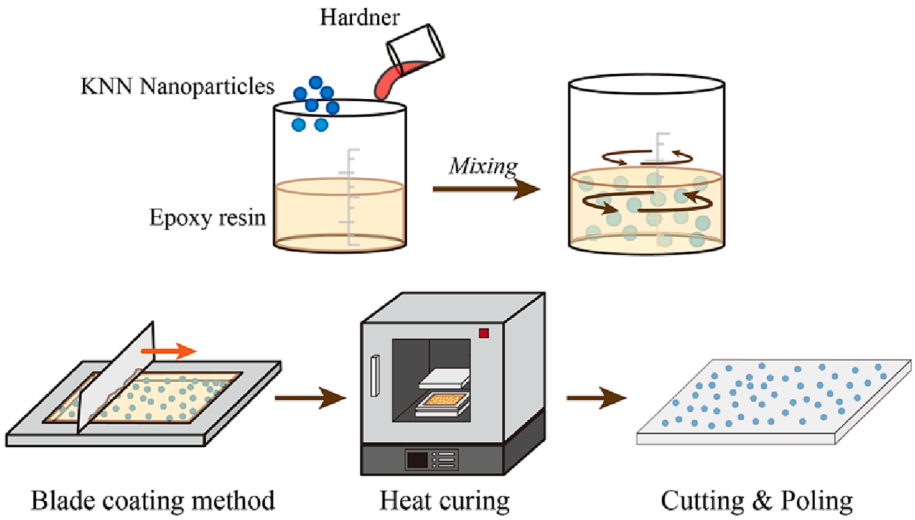

Fig. 1. Fabrication of KNN-nanoparticle-filled epoxy (KNN–EP) plate.

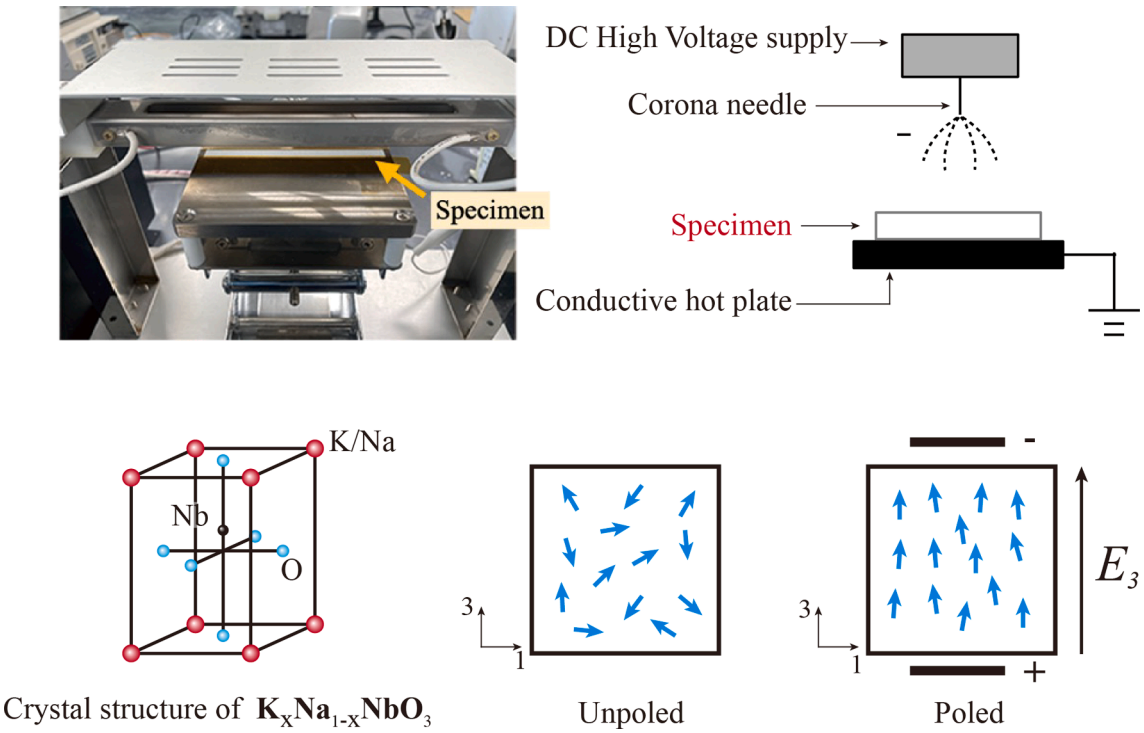

Fig. 2. Specimen setup and working mechanism of the poling process (E_3 represents the electric field intensity vector).

composites also in addition to electrical energy generation and mechanical deformation sensing. Piezoelectric composites are promising materials for SHM applications because they enable the detection and monitoring of structural integrity changes, such as the development of cracks or delamination [22]. When mechanical properties change within the composite material, piezoelectric components generate precise electrical signals that can be measured and analyzed, providing valuable information regarding the composite material condition. Yuan et. al. [23] developed a piezoelectric-filled nanofiber membrane sensor using polyacrylonitrile and 15 wt% barium titanate nanoparticles for real-time damage detection in composites. The sensor exhibited stress–strain and voltage–time curves during bending with a saw-tooth pattern, indicating delamination damage. Developing piezoelectric composites for SHM requires a deep understanding of their mechanical, electrical, and piezoelectric properties. This has spurred research into modeling and simulation techniques as well as fabrication and testing methods to fully exploit the unique capabilities of these materials [24].

Wang et al. [25] proposed a strategy for laminating CFRP with 0–3 type piezoelectric polymers for developing energy harvesting structures. This piezoelectric hybrid CFRP composite material can be used as self-powered sensors in SHM. While there have been advancements in utilizing CFRP within piezoelectric composites, certain obstacles still need to be overcome. These include finding solutions to the problems of low output voltage and high resistance. Additionally, it is important to investigate methods for improving signal processing of the output voltage. One potential approach is to utilize technologies, such as the fast Fourier transform (FFT) and the wavelet transform (WT), which can minimize noise interference and improve the precision of information extraction [26].

To address these challenges, this study proposes a combination

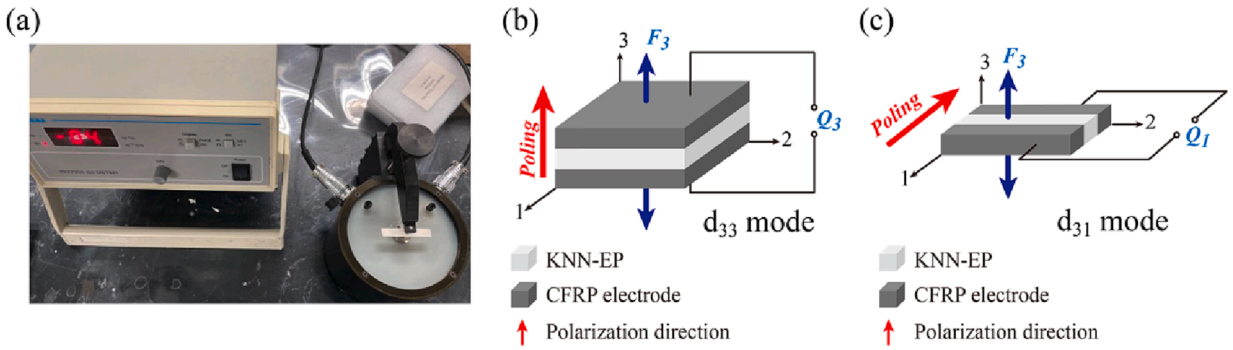

Fig. 3. (a) Digital photograph of piezo-meter. (b) and (c) Mechanism of the piezoelectric coefficients, d_{33} and d_{31}, respectively.

strategy involving a lead-free sodium potassium niobate ($K_xNa_{1-x}NbO_3$: KNN)-nanoparticle-filled epoxy (EP) plate with CFRP to enhance the mechanical strength of the sensor and achieve electrical conduction. The piezoelectric laminate beam theory is used to calculate the electromechanical properties through a cyclic 3-point bending test. The test involves the evaluation of structural precrack monitoring and kinetic energy generation based on structural dynamic response changes. The results indicate that the KNN–EP plate with CFRP electrodes has greatly improved the output performance while sensitively responding to precrack growth and damage behaviors.

2. Material and methods

2.1. Fabrication of the KNN–EP composite

Fig. 1 shows the fabrication of KNN–EP plate. Three volume fractions (V_f = 25, 30, and 35 vol%) of the $K_{0.5}Na_{0.5}NbO_3$ nanoparticles (Nippon Chemical Industry Co., ltd., Japan) were tested in the composite. In the manufacturing process of the 0–3 piezoelectric composite material, the content of piezoelectric particles determines the piezoelectric performance of the composite material. However, significantly high filler content will hinder the production and lead to quality deterioration. These KNN volume fractions were selected based on a previous experiment [27] and the optimal ratio of the KNN nanoparticles to the EP resin was found to be approximately 30 vol%. The composite was fabricated through the following process. (i) The KNN nanoparticle-filled bisphenol-F EP resin (Daido Co., ltd., Japan) was mixed using a planetary mixer for 60 min. (ii) The hardener (Mitsubishi Chemical Co., ltd., Japan) was then added and mixed for 10 min, and the mixture was deformed for 5 min. (iii) The uncured resin was uniformly coated based on the blade coating method using a 0.5-mm mold. (iv) The resin was then cured by heating in a vacuum oven (DVS402, Yamato Scientific Co., ltd., Japan) at 80 °C for 3 h.

2.2. Poling process

The most important class of piezoelectric materials has an off-centered atom in its crystal structures, which allows the unit cell to have a spontaneous polarization and to exhibit a spontaneous strain alignment with the dipole moment of the charge distribution. The piezoelectric property is the ability of a material to generate an electric charge in response to an applied mechanical stress. During polarization, the material is subjected to a very high electric field, which orients all dipoles in the direction of the field [28]. Fig. 2 shows corona-poling equipment (ELC-01 N, Element Co., ltd., Japan), which is used to impart piezoelectric properties to the KNN–EP plate through the following process. (i) The specimens were initially heated to 75 °C on a conductive hot plate. (ii) A direct current (DC) electric field (electric field strength = 20 kV/mm) was supplied using a poling system along the thickness direction for 60 min. (iii) The specimen was cooled to room temperature while maintaining the poling electric field. To investigate the relationship between the poling time and piezoelectric effect, the longitudinal piezoelectric coefficient d_{33} (the subscript of d_{33} represents the vibration mode) was measured every 10 min.

2.3. Piezoelectric coefficient

Measurements were taken to determine the longitudinal and transverse piezoelectric coefficients. Fig. 3 displays photographs of the piezometer, as well as the schematic diagrams illustrating the longitudinal piezoelectric coefficient, d_{33}, and the transverse piezoelectric coefficient, d_{31}.

Longitudinal piezoelectric coefficient, d_{33}

Fig. 3a shows a digital photograph of the piezoelectric coefficient measurement and a schematic of the mechanism of the piezoelectric coefficient. The longitudinal piezoelectric coefficient d_{33} is a significant parameter, which determines the conversion efficiency between the electrical and mechanical energy for piezoelectric sensors that operate under a longitudinal mode.

The rectangular Cartesian coordinates x_i (x_1, x_2, x_3) were considered. The constitutive relations of piezoelectric materials poled in the x_3-direction can be found in Appendix A. Let the thickness direction of the KNN–EP plate shown in Fig. 3b be x_3-axis. For a one-dimensional model, the constitutive equations (A.1) and (A.2) can be expressed as follows:

$$\varepsilon_{33} = s_{33}\sigma_{33} + d_{33}E_3 \tag{1}$$

$$D_3 = d_{33}\sigma_{33} + \epsilon^{\mathrm{T}}_{33}E_3 \tag{2}$$

When the stress, σ_{33}, is applied in the direction of the polarization axis, x_3, electric displacement, D_3, occurs. The electric field, E_3, is assumed to be constant (for example, E_3 = 0) in Eq. (2). The electric displacement is estimated by $D_3 = Q_3/A$, where A is the electrode area and Q_3 is the surface charge (Fig. 3b). Since $\sigma_{33} = F_3/A$, the piezoelectric coefficient d_{33} is obtained as

$$d_{33} = \frac{D_3}{\sigma_{33}} = \frac{Q_3\sin(\omega t)}{F_3\sin(\omega t)} \tag{3}$$

where F_3 is the x_3 component of the force vector, ω is the angular frequency, and t is the time. An alternating current load ($F_3\sin(\omega t)$, N) was applied to the specimen from the holder of the probe, and an alternating charge ($Q_3\sin(\omega t)$, C) was generated between the electrodes of the sample. This results in the generation of a corresponding charge with an alternating force and fixed amplitude. A piezo-meter was utilized to determine the longitudinal direct piezoelectric coefficient.

Transverse piezoelectric coefficient, d_{31}

The transverse piezoelectric coefficient, d_{31}, primarily indicates the relationship between the induced charge on the piezoelectric material and the applied load F_3, which is perpendicular to the polarization direction x_1 as illustrated in Fig. 3c. It specifically quantifies the material's

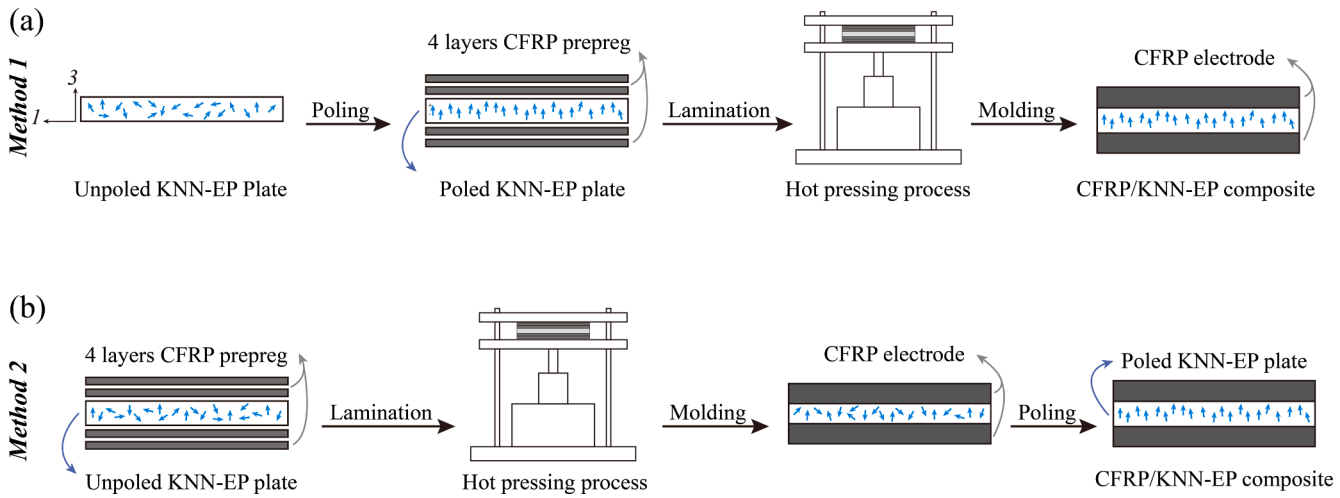

Fig. 4. (a) Method 1 for the composite fabrication, in which the poling treatment is followed by the lamination and molding steps; (b) Method 2 for the composite fabrication, in which the poling treatment is conducted after the lamination and molding steps.

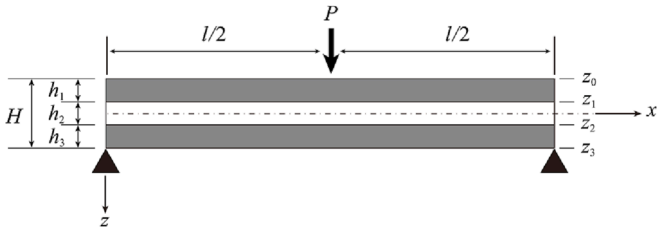

Fig. 5. Schematic of a center-loaded piezoelectric laminated beam for the 3-point bending test.

transverse piezoelectric response; here, electric displacement D_1 is perpendicular to the stress σ_{33}. Thus, the piezoelectric coefficient, d_{31}, is obtained as follows.

$$d_{31} = \frac{D_1}{\sigma_{33}} = \frac{Q_1 \sin(\omega t)}{F_3 \sin(\omega t)} \tag{4}$$

Note that the constitutive relations of piezoelectric materials poled in the x_1-direction cannot be shown in this paper.

2.4. Assembly of the CFRP electrodes

Since the general piezoceramic particles dispersed in a polymer matrix (type 0–3 piezoelectric composites) are brittle, these materials are generally difficult to use as structural components. The CFRP layer, with excellent mechanical properties and conductivity, is suitable for the electrode. The d_{33} value, which represents the charge generated by the functional layer under external force, was measured to determine whether the CFRP electrode can work. A poor-quality CFRP will result in an inhomogeneous d_{33} distribution.

The woven CFRP prepreg molding process (F6347B-05P #2500, TORAY Industries, Inc., Japan) requires high temperature and pressure. According to a previous study [27], the piezoelectric properties are sensitive to temperature, causing significant depolarization phenomena and weakening the piezoelectric output performance. Therefore, two methods were proposed in this work for the fabrication of the composite and are discussed below. The length L, width b, and thickness H of the developed CFRP/KNN–EP composite specimen are approximately 30, 5, and 1.5 mm, respectively.

Method 1: The poling process was conducted followed by the lamination and molding steps (Fig. 4a). (i) The KNN–EP plate was poled at 75 °C and 20 kV/mm for 60 min, and the electric field was maintained until the film was cooled to room temperature. (ii) Two CFRP prepreg layers were laminated on the upper and lower surfaces of the KNN–EP plate. The laminated composite material was then cured under pressure at 126 °C. To explore the effect of the molding pressure on the electrical conductivity of the composite, the electrical conductivities were compared under different molding pressure values (i.e., 1, 3, 5, and 10 MPa). These pressure values were selected by referring to the prepreg worksheet. However, according to the preliminary experiments, the inflection point of the Young's modulus usually occurs under approximately 5 MPa because excessive pressure causes the resin to overflow. Moreover, excessive pressure also causes fiber scattering, resulting in poor molding quality.

Method 2: As shown in Fig. 4b, the poling treatment was performed after the completion of the CFRP molding to avoid the depolarization caused by high temperature and pressure. (i) The unpolarized KNN–EP plate and CFRP prepregs were laminated and cured. The molding conditions were the same as in Method 1. (ii) A KNN–EP plate equipped with CFRP electrodes was subjected to poling under the same conditions as in Method 1. This method prevented the depolarization of the piezoelectric layer due to high temperature of the CFRP molding.

2.5. Measurement and characterization

A piezo-meter (YE2730A, Sinocera Piezotronics Inc., China) was used to determine the piezoelectric coefficients, d_{33} and d_{31}. The particle distribution and molding quality of samples with varying KNN content were examined using scanning electron microscopy (SEM, SU-70, Hitachi High-Tech Co., Japan). The crystal structure of the KNN–EP plate was characterized using X-ray diffraction with K β radiation (operating at 40 kV and 40 mA; $\lambda = 1.54$Å; and $2\theta = 20^{\circ} - 60^{\circ}$, SmartLab SE, Rigaku Co., Japan). The 3-point bending test was conducted on a universal machine (Autograph AGS-X, Shimadzu Co., Japan). In addition, the output signals of this piezoelectric composite were obtained using an electrometer (model 6514, Keithley Instruments, Inc., USA) and a datalogger system (NR-500, Keyence Co., Japan) under cyclic bending. FFT-based analysis and the WT have been employed for signal processing using numerical-analysis software MATLAB.

2.6. 3-point cyclic bending for energy harvesting and end-notched flexure (ENF) test

Since the piezoelectric sensors can convert mechanical energy into electrical energy, energy can be harvested from traffic-induced vibrations [29]. Thus, the response of the piezoelectric sensor to mechanical

Table 1
Specifications of the 3-point cyclic bending and ENF tests.

Specification	Notation	Size (mm)
Length of specimen	L	30
Support span	l	20
Width of specimen	b	5
Thickness of specimen	H	1.5
Thickness of upper CFRP electrode	h_1	0.5
Thickness of KNN–EP	h_2	0.5
Thickness of lower CFRP electrode	h_3	0.5
Initial crack length	a	10

variations was investigated. The 3-point bending test was performed using a universal testing machine (Autograph Ag-50KNXD, Shimadzu Co., ltd., Japan). The monotonic 3-point bending test speed is controlled at 0.1 mm/s.

To evaluate the bending strength, the bending stress of the CFRP/KNN–EP composite was derived. Fig. 5 shows a schematic of 3-point bending specimen with concentrated load P and span l. The constitutive relations of a piezoelectric material are given in Appendix A. Let the coordinate axis $x = x_1$ and $y = x_2$ be chosen to coincide with the composite beam's middle plane and the $z = x_3$ axis is perpendicular to this plane. CFRP electrode layers are added to the upper and lower surfaces of a KNN–EP plate poled in the z-direction. The total thickness is H, and the kth layer has a thickness $h_k = z_k - z_{k-1} (k = 1, 2, 3)$. h_1 and h_3 are the thicknesses of the CFRP electrodes, and $h_2 = H - (h_1 + h_3)$ is the thickness of the KNN–EP layer. The constitutive equations for the kth layer can be found in Appendix B.

The bending stress at the interface between the upper CFRP and KNN–EP layers, $(\sigma_{xx})_2$, and the maximum bending stress $(\sigma_{xx})_3$, is given by

$$(\sigma_{xx})_2 = z_1\left[(\bar{Q}^p_{11})_2 D^*_{11} + (\bar{Q}^p_{12})_2 D^*_{12}\right] M_{xx} \tag{5}$$

$$(\sigma_{xx})_3 = z_3\left[(\bar{Q}^{cf}_{11})_3 D^*_{11} + (\bar{Q}^{cf}_{12})_3 D^*_{12}\right] M_{xx} \tag{6}$$

where D^*_{11} and D^*_{12} are the bending stiffness of the laminated CFRP/KNN–EP beam given in Appendix B, and z_k is the distance from the neutral plane. The bending moment is given as follows:

$$M_{xx} = \frac{Px}{2} (0 \le x \le l/2) \tag{7}$$

In the cyclic bending test, the load, P, is controlled between its minimum and maximum values and is applied on the center of the specimen at a bending rate, v. The specimen specifications used in the 3-point bending testing are listed in Table 1. The output voltage signals and peak-to-peak output voltage, V_{pp}, were recorded using a data logger (NR-500, Keyence Co., Japan). The relationship between the open-circuit electric field $(E_x)_2$ (at $D_z = 0$) of a d_{31}-mode CFRP/KNN–EP composite and an applied mechanical stress $(\sigma_{xx})_2$ can be obtained approximately using the following equation:

$$(E_x)_2 = -\frac{d_{31}}{\epsilon^T_{33}} (\sigma_{xx})_2 \tag{8}$$

Bending leads to lateral straining of the piezoelectric material and decreases its polarization [19]. In this case, a potential difference (built-in electric field, E_z) is created, and positive and negative electrical signals are generated by the bending strain increases and decreases.

The interfacial adhesion strength between the KNN–EP plate and the woven CFRP laminate was evaluated using a 3-point bending test method and cross-section observation via photographs. The results indicated that the KNN–EP plate and the woven CFRP laminate exhibited good adhesion strength. Hence, a piece of Teflon sheet (length = 10 mm, width = 5 mm, and thickness = 20 μm) was placed between the CFRP layer and the piezoelectric layer to characterize the crack growth of the CFRP/KNN–EP composite for SHM. To determine the relationship between the crack growth and output voltage signals of these stacked layers of different materials, an ENF test was conducted (Fig. 6). The coordinate axes, x and y, are at the bottom surface of the CFRP/KNN–EP composite, and the $z = x_3$ axis is normal to this plane. Initial crack length is a. The specimen specifications used in the ENF testing are listed in Table 1.

Before the 3-point cyclic bending for energy harvesting and the ENF test, a 3-point bending test was conducted to investigate bending properties of a CFRP/KNN–EP composite. The experiment followed the JIS K 7017 standard, except for the specimen thickness, where a 2/5th size variation from the standard was used.

3. Results and discussion

3.1. Effect of the volume fraction of KNN on d_{33} and the mechanical properties of the composite

The blade coating method used in this study achieved a large area of one-time molding. Although the large size of the KNN–EP layer is convenient for covering differently sized sensors, the uniformity of mixed resin must be considered. For piezoelectric materials, d_{33} is the most important parameter as it determines the piezoelectric performance in the thickness direction. Previous studies only presented the

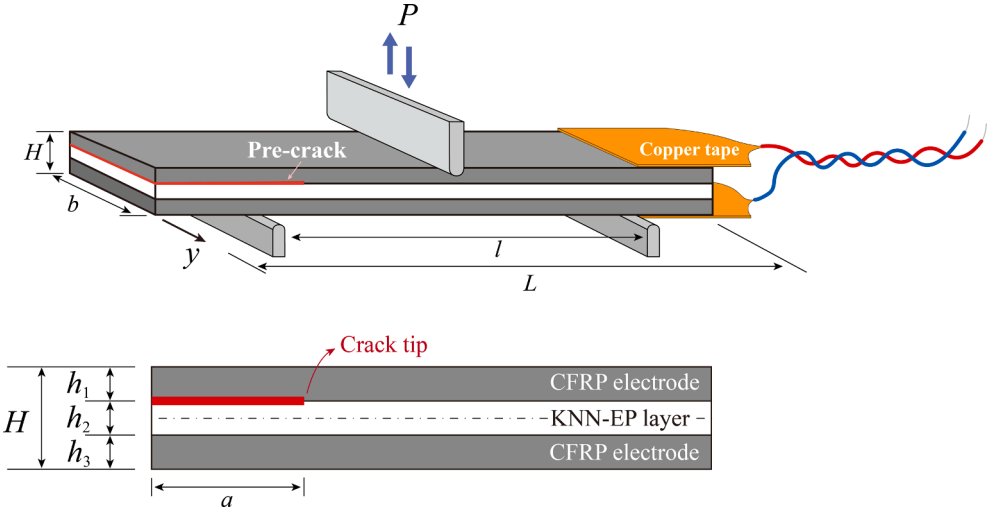

Fig. 6. Schematic diagram of the energy harvesting and ENF experimental setup.

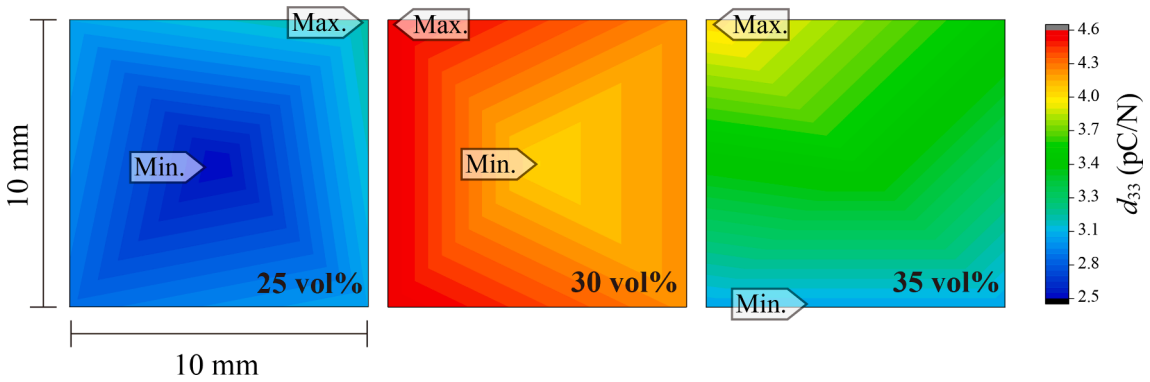

Fig. 7. d_{33} values of the specimens at different KNN volume contents.

Table 2
Comparison of the piezoelectric coefficient of KNN-nanoparticle-filled composites.

Filler	Matrix	Content	d_{33} (pC/N)	d_{31} (pC/N)	
KNN	Epoxy	30 vol%	5.0	−3.0	This work
KNN	GFRP/Epoxy	20 vol%	3.5	–	[30]
KNN	PVDF	40 vol%	10	–	[31]

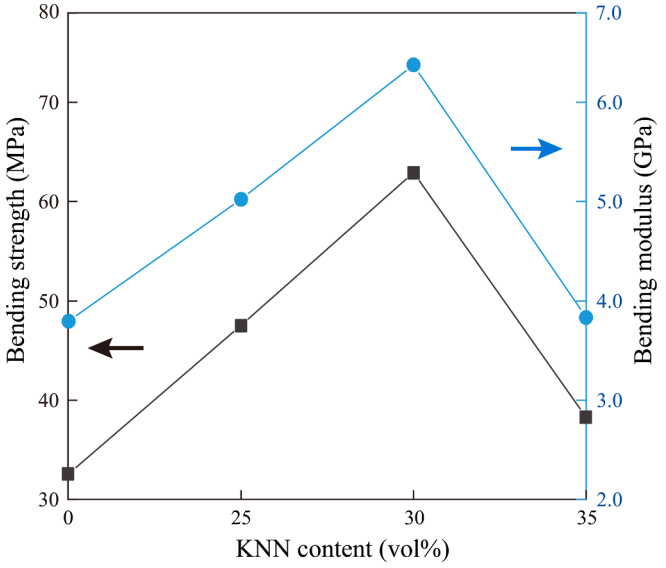

Fig. 8. Bending properties of the KNN–EP plates with different KNN contents.

average value of the samples. To investigate the uniformity, each 10 mm × 10 mm specimen was divided into nine areas for the d_{33} test, and then collected and graded.

The uniformity of the specimens can be rapidly evaluated using the figure proposed in this work after visualizing the d_{33} results. Fig. 7 presents a distribution map of the d_{33} values of the specimens at KNN contents of 25 vol% – 35 vol%. The positions of the maximum and minimum values of d_{33} have been marked on the figure, and the difference is expressed as Δd_{33}. This pattern suggests that the specimens with 25 vol% ($\Delta d_{33} = 0.6$ pC/N) and 30 vol% ($\Delta d_{33} = 0.5$ pC/N) do not show significant inhomogeneity or unevenness, whereas the sample with 35 vol% shows a decrease in the average d_{33} value (~3.5 pC/N) and uniformity ($\Delta d_{33} = 1.1$ pC/N). Although composites with higher volume fractions of the piezoelectric nanoparticles should further increase the piezoelectric performance, they degrade the quality of the specimen, reducing its mechanical and piezoelectrical properties. This result indicates that the sample with 30 vol% KNN nanoparticles has the highest d_{33} value (~4.5 pC/N) and shows an overall good equality, which provides a good basis for a high voltage signal output. Table 2 lists the piezoelectric coefficients d_{33} and d_{31} of KNN–EP plate in this study. The piezoelectric coefficient d_{33} of KNN–EP/CFRP composite was also compared with KNN piezoelectric composites of other studies.

Fig. 8 shows a comparison between the bending properties of KNN–EP plate. Although adding KNN nanoparticles relatively enhances the mechanical performance ($E_{11}^{piezo} = 6.2$GPa in 30 vol% KNN content) of the specimens, an excessive KNN content significantly reduces it. This can be attributed to the incompatibility between the KNN nanoparticles and EP resin matrix. This incompatibility causes void formation and aggregates, which can act as defects, reducing the mechanical properties of the composites. Therefore, all the following tests were conducted using the 30 vol% KNN content.

SEM was utilized to observe the microscopic images of the KNN–EP plate and to analyze the dispersion uniformity of KNN nanoparticles with varying volume contents. The effect of KNN nanoparticle content on the microstructure of the piezoelectric composites was also investigated, as illustrated in Fig. 9. Results indicated that the aggregation of piezoelectric nanoparticles can create challenges in fabricating composites and negatively impact their mechanical properties. Notably, an increase in KNN content above 35 vol% resulted in an increase in nanoparticle agglomeration, along with a significant increase in voids between the EP resins, as indicated by the presence of black cavities. These findings underscore the importance of controlling the volume content of KNN nanoparticles in piezoelectric composites to prevent agglomeration and maintain the preferred microstructure and mechanical properties of the composites.

3.2. *Effect of the CFRP molding temperature on polarization*

Among the lead-free piezoelectric perovskite materials, KNN-based materials have been extensively studied due to their excellent piezoelectricity and high Curie temperature, T_c [32,33]. Below the Curie temperature, the crystal of the KNN-based materials becomes tetragonal (rectangular parallelepiped) or orthorhombic. In a tetragonal crystal, the *c*-axis is longer than the other two axes ($a = b \neq c$), and all its angles are 90° ($\alpha = \beta = \gamma = 90°$, where α, β, and γ are the angles between *b* and *c*, *a* and *c*, as well as *a* and *b*, respectively). Conversely, the angles of the orthorhombic crystal are equal, and the lengths of the axes are different ($a \neq b \neq c$). A typical tetragonal crystal of the KNN materials exhibits an elongated *c*-axis and a higher electrically unbalanced dipole moment [34]. However, some disadvantages still exist such as the poor temperature stability of the materials. Fig. 10a shows the XRD patterns of the crystal structure of KNN nanoparticles. In addition, CFRP prepreg on the market is mainly divided into low-temperature type 126 °C and high-temperature type 177 °C to meet the demands of different fields. Therefore, these two temperatures are used as conditions for heat resistance tests. XRD peak of an unpoled KNN nanoparticle is observed

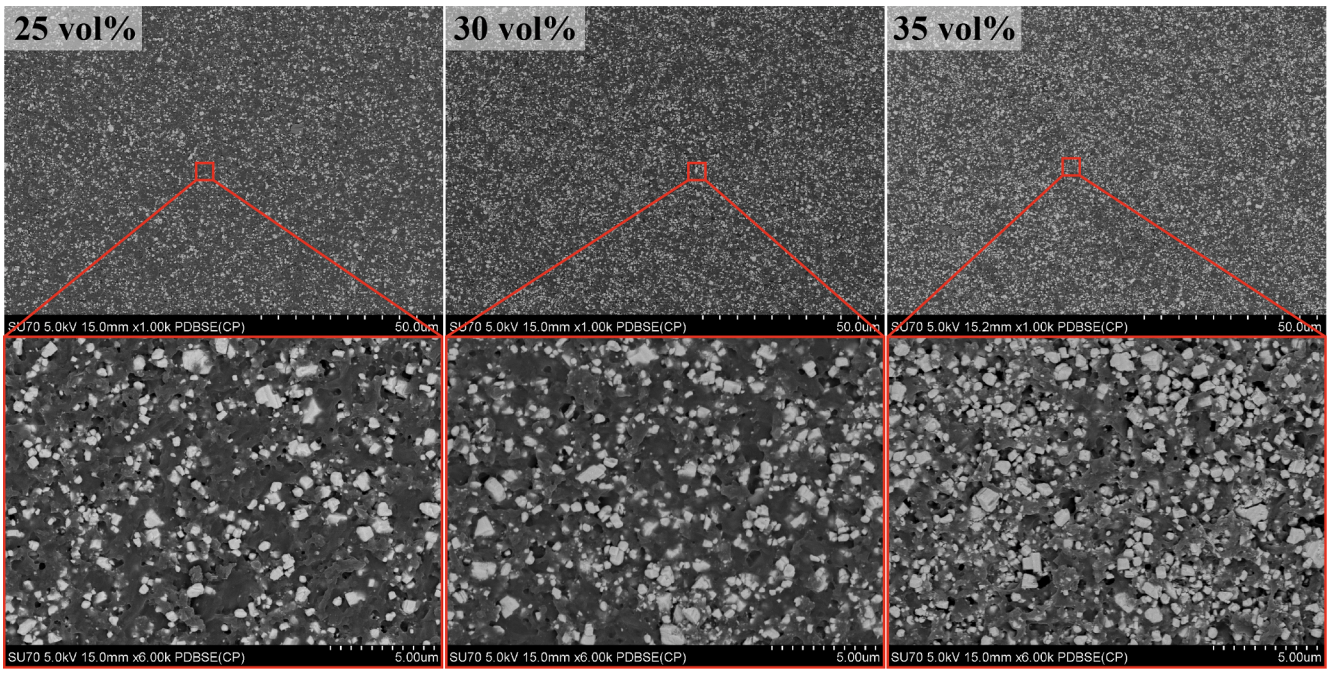

Fig. 9. SEM images of piezoelectric composites with different KNN contents.

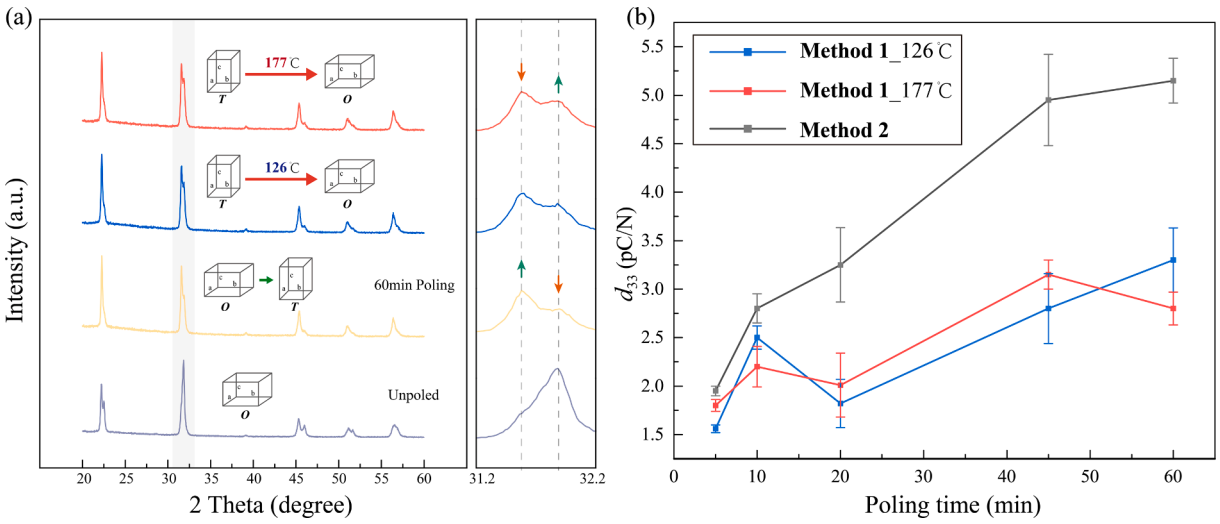

Fig. 10. (a) XRD patterns of the KNN nanoparticles. (b) Effect of a high-temperature environment on the piezoelectric coefficient.

at approximately $2\theta = 32^{\circ}$ with a peak splitting at approximately $2\theta = 22^{\circ}$ and 45°, which corresponds to the orthorhombic phase. After a suitable poling treatment, the peak corresponds to the tetragonal phase, and the peak splitting decreased. Furthermore, after heating the KNN–EP plate for 60 min, the intensity of the peak splitting at $2\theta = 32^{\circ}$ increased, indicating the tetragonal phase shift to the orthorhombic phase. In the experiment, CFRP electrodes were assembled by hot pressing, leading to depolarization and poor piezoelectric performance ($d_{33} < 3.0$ pC/N, Fig. 10b). To avoid depolarization caused by high temperature, Method 2 ($d_{33} \sim 5$ pC/N) is more suitable for the composite fabrication.

3.3. Effect of the CFRP molding pressure on the poling treatment and piezoelectric properties

Although carbon fiber is a good conductor, the polymer matrix in CFRP is an insulator. Therefore, when CFRP is used as an electrode, the carbon fibers should be in good contact with each other. The molding pressure is a key factor in the fabrication process because it affects the fiber to matrix ratio. Thus, using a suitable pressure guarantees good contact between the internal carbon fibers. Fig. 11a shows the molding temperature–pressure graph of the CFRP electrode. Fig. 11b shows the bending properties of the CFRP electrodes under different molding pressures, demonstrating that the CFRP electrodes molded under high pressure have a higher modulus, $E_{11}^{cf} = 54.9$GPa under 5 MPa molding pressure. In contrast, the bending strength of the CFRP electrodes decreases at high pressures. Fig. 11c shows the variations in the electrical resistance of the CFRP electrode and piezoelectric coefficient of the CFRP/KNN–EP composite under different molding pressures. As expected, the electrical resistance of CFRP decreases with the increase in the pressure. In contrast, no significant correlation was observed between the electrical resistance and d_{33}. Comparing Fig. 11b and c, the d_{33} values are consistent with the variation in the bending properties. Although the resistance of the electrodes also affects the output

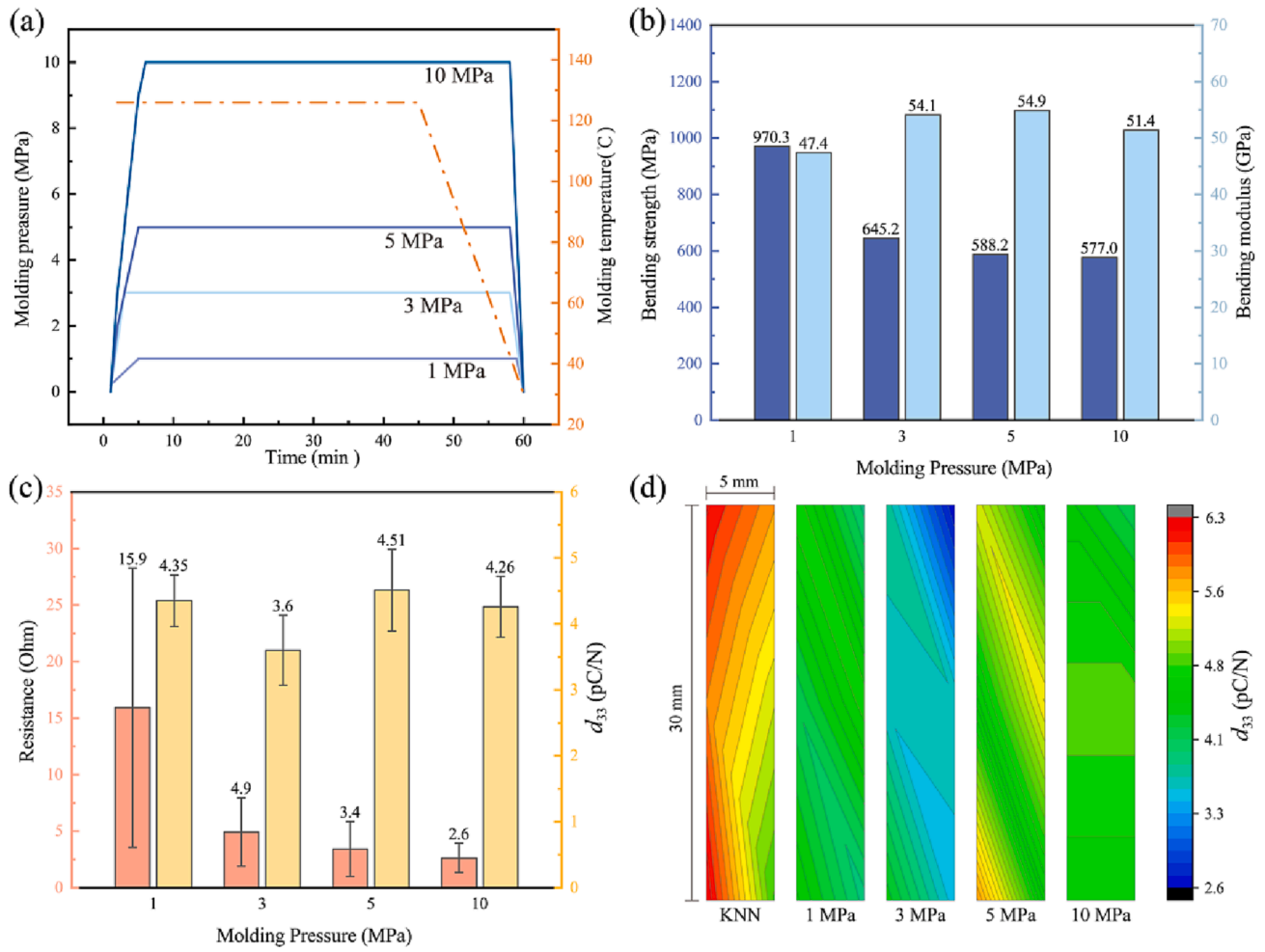

Fig. 11. (a) CFRP electrode molding conditions. (b) Bending strength and modulus of the CFRP electrodes under different molding pressures. (c) Resistance of the CFRP electrode in the thickness direction, and the average d_{33} value. (d) Distribution of the d_{33} values of CFRP/KNN–EP.

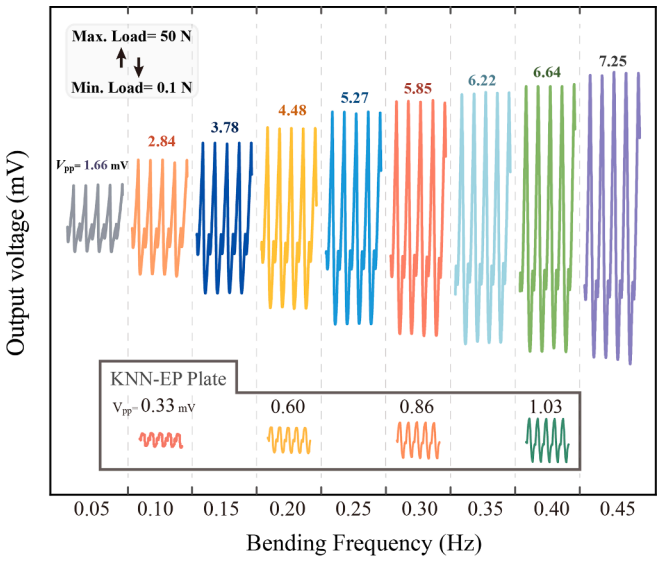

Fig. 12. Output voltage signals generated by CFRP/KNN–EP. The inset represents those generated by the KNN–EP plate.

performance of the piezoelectric layer, the effect is slight when the electrical resistance is below 50 Ohm. Fig. 11d shows the d_{33} distribution map after the assembly of the CFRP electrodes. The resin in the CFRP electrode may harm the uniformity. Fortunately, the results show that although d_{33} is slightly decreased, the material uniformity is maintained.

3.4. Output performance of CFRP/KNN–EP evaluated through a cyclic 3-point bending test

The electrical output performance of the CFRP/KNN–EP composite was investigated by a cyclic 3-point bending test at an increasing frequency (0.05 –0.45 Hz) under a load of 0.1–50 N. As shown in Fig. 12, the V_{pp} increases from 1.66 to 7.25 mV with the increase in the bending speed. It is noteworthy that the CFRP/KNN–EP composite has the potential to be used as a self-powered sensor. The output voltage is proportional to the bending frequency because the bending frequency is significantly lower than the natural frequency. In addition, the graph shows that the CFRP/KNN–EP composite can output a stable voltage signal under cyclic bending at every stage, and it can be used as a basis for damage detection.

The output voltage of the KNN–EP plate without the CFRP electrode (inset in Fig. 12) was compared to that of the composite, and the results showed that the output performance of the composite was significantly improved (over 600 %). The reason for this is that the effect of the reduction in the piezoelectric coefficient on the output performance is lower than the performance improvement due to the enhancement of the

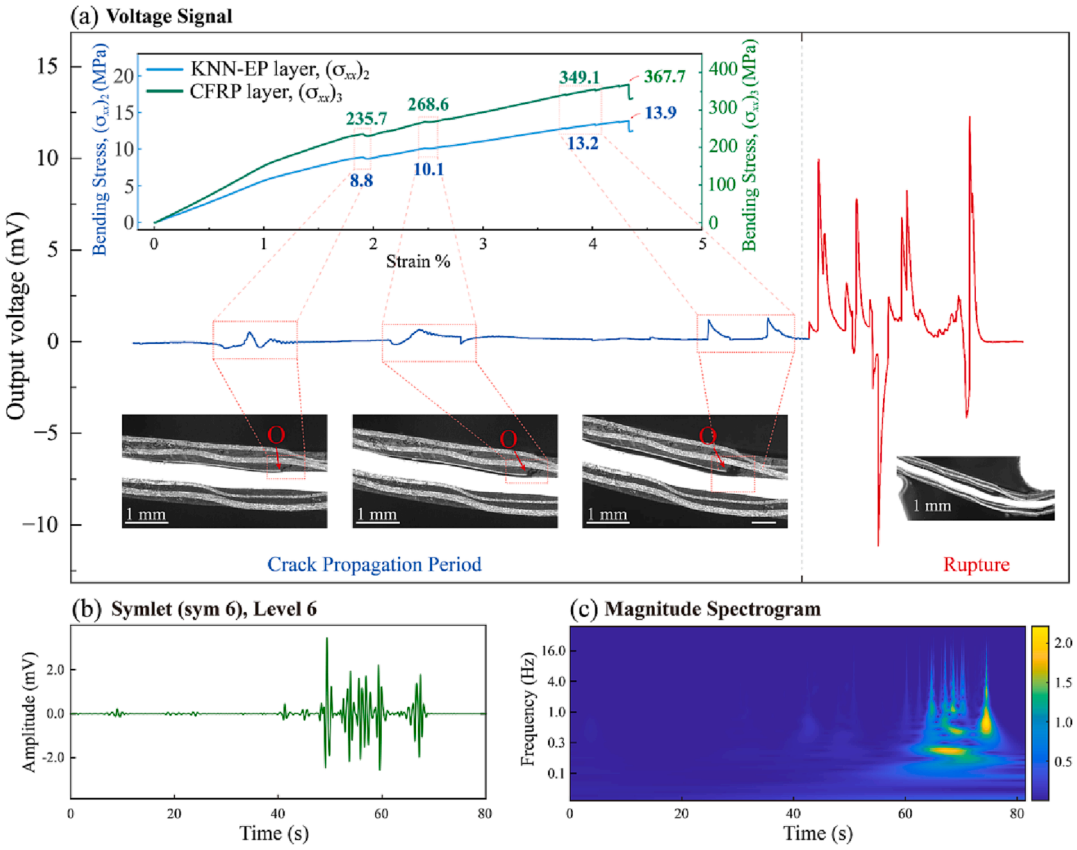

Fig. 13. Case 1: using ENF CFRP/KNN–EP for damage detection in a monotonic bending test. (a) Voltage signal, the insets are bending stress versus strain curve and cross-sectional observation. (b) Symlet wavelet transform plot. (c) Magnitude spectrogram (unit: mV) of the raw time signal.

mechanical properties of the composite due to introducing CFRP.

3.5. *Using ENF CFRP/KNN–EP for testing, nondestructive evaluation, and damage detection*

Piezoelectric materials are functional materials that can respond to different electrical signals as a result of changes in the external force. This principle can be used to detect crack propagation in materials and evaluate structural health. In the theoretical model used in this experiment, precrack was not located in the middle of the sample, and cracking at the crack tip was expected to be a mixed mode containing Mode I and Mode II. Moreover, the direction of crack development was not completely parallel. Therefore, the theoretical calculation of crack propagation was complex.

However, considering the characteristics of carbon fiber composites with plain texture structures, it fractures when cracks develop in the thickness direction. When the crack development direction is transverse, the crack mainly propagates in the resin matrix, and the fiber does not fracture significantly. Based on this characteristic, when the piezoelectric material releases a small and short peak signal, it can be inferred that longitudinal crack propagation has occurred in the CFRP. Conversely, if the piezoelectric signal shows a longer period and a significant increase in amplitude, it can be concluded that the direction of crack propagation is primarily in the transverse direction between resins and is consistent with the direction of the bending stress. Therefore, the use of piezoelectric materials in this experiment is a reliable method to detect crack propagation and analyze the health of the structure.

Fig. 13a shows the first testing case (Case 1), which is a monotonic bending test using an ENF specimen. CFRPs are used to reinforce concrete bridges by being placed in the bottom part. Therefore, when the bridge is subjected to an external deformation force, the situation is similar to the 3-point bending. In this situation, failure mode II (i.e., ENF) problems are worth noting, including internal delamination of CFRP and interfacial adhesion. Here, since it is difficult to discuss the damage behavior in terms of the cracked piezoelectric composite materials' bending stress, the bending stress acting on the virtual crack plane and the maximum bending stress are used. The voltage signal indicates that the maximum bending stress acting in the absence of a crack, $\sigma_{max} = (\sigma_{xx})_3$, increases to 235.7 MPa, and the sensor generates feedback (a peak) for the first time when the bending stress on the virtual crack plane $(\sigma_{xx})_2$ is 8.8 MPa at a loading speed of 0.1 mm/s. Then, the crack growth can be observed at the crack tip. Next, the feedback of the electrical signals is obtained at$(\sigma_{xx})_3 = 268.6$ MPa, $(\sigma_{xx})_2$=10.1 MPa and$(\sigma_{xx})_3 = 349.1$ MPa, $(\sigma_{xx})_2$=13.2 MPa, which also corresponds to the crack growth. With further increase in the deflection of the loading point, the bending and shear stress near the initial crack tip exceed the critical value. This stage of the crack propagation sequence corresponds to the generated voltage signal peaks (Fig. 13b). Finally, multiple voltage signal peaks are detected in Fig. 13c because of the continuous fracture development in the CFRP/KNN–EP composite during the monotonic bending when the $(\sigma_{xx})_3$ and $(\sigma_{xx})_2$ developed to 367.7 MPa and 13.9 MPa, respectively. Notably, in the monotone bending experiment, the bending stress of the KNN–EP is still lower than the bending strength shown in Fig. 8 until the specimen ruptured, indicating that the CFRP layer greatly improved the applied force range of the CFRP/KNN–EP composite. Moreover, although the KNN–EP layer is in the neutral plane, the sensitive sensing function can still be maintained.

In the second case (Fig. 14), ENF specimens were tested under cyclic bending. Fig. 14 shows the results when the load P_{max} is increased to 90 and 100 N (the $\sigma_{max} = (\sigma_{xx})_3$ is 247.1 MPa and 274.5 MPa, respectively). The crack initiation period ended at 90 N with a stable voltage signal ($V_{pp} = 1.75$ mV). When the load P_{max} increases to 100 N, the crack grows

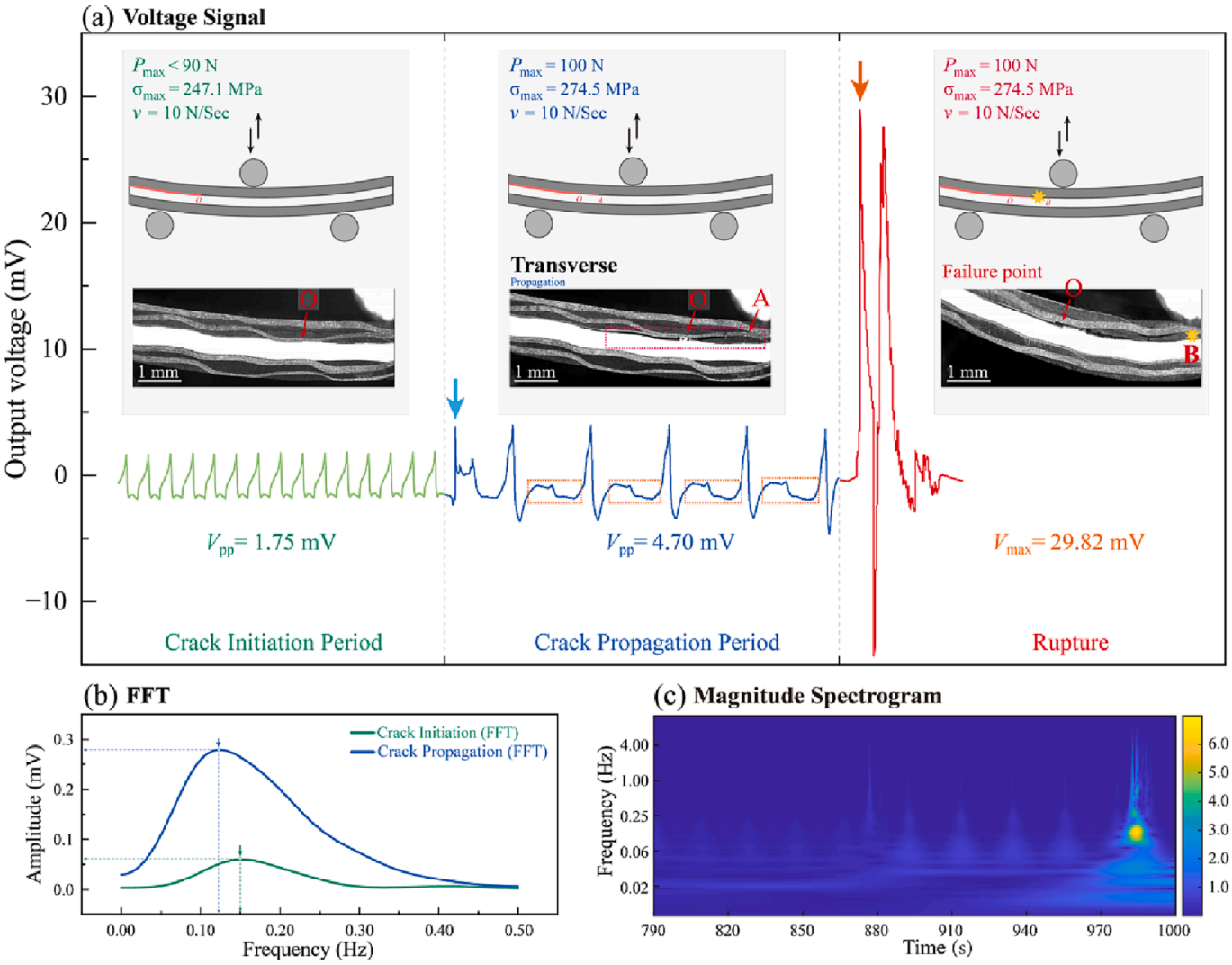

Fig. 14. Case 2: using ENF CFRP/KNN–EP for damage detection in a cyclic 3-point bending test. (a) Voltage signal, the inset is cross-sectional observation. (b) FFT spectrum analysis, and (c) magnitude spectrogram (unit: mV).

to point A. At this time, the V_{pp} increases to 4.7 mV because crack propagation reduces the stiffness of the sample, $E_{11}^{c}I^{c}$, leading to an increase in the load-point deflection, δ, under the same load. In addition to the obvious increase in the peak voltage, the period of the electrical signal within the marked range increased significantly as the crack begins to extend under cyclic load (see the range of orange squares in Fig. 14). Fig. 14b compares the FFT of the voltage signal for the crack initiation and propagation periods. The frequency of the crack initiation period was 0.15 Hz, which corresponds to the bending frequency. In the propagation period, the signal amplitude increased considerably, whereas the frequency decreased. At the same bending rate, the time to reach the target load increased, which coincides with an increase in the output voltage signal path to the peak value. Therefore, the iconic signal paths proved crack propagation and indicated a rupture was about to occur. Eventually, a voltage signal peak occurred when a rupture occurred, as shown in Fig. 14c.

The observation of the voltage signals and fracture through the cross-section indicates that the voltage signal is also related to the crack propagation direction. The left cross-section photo in Case 3 (Fig. 15) shows a longitudinal crack growth under a load P_{max} of 70–80 N, which the $\sigma_{max} = (\sigma_{xx})_3$ is from 192.2 MPa to 219.6 MPa. Moreover, the electrical signal exhibits slight irregular vibrations near the peak position with no growth in the signal path. The voltage signal could be ascribed to the longitudinal crack growth perpendicular to the direction of the CFRP prepreg lamination, causing fiber breakage, which corresponds to these slight signal vibrations (Orange square). As shown in the right cross-section photo, the crack grows in the horizontal direction as the cyclic bending continues. Owing to the horizontal crack growth in the polymer matrix, the energy release rate and the crack sliding displacement rapidly increase with the load, showing further development of the signal patterns (sky blue range). Conversely, the signature electrical signal path also appears during the transverse crack growth. Compared with crack initiation and longitudinal propagation, the signal period during transverse propagation is significantly longer. Fig. 15b records the FFT plots of the voltage signal to explain the evolution of the spectrum over time. The signal exhibits the first harmonic peak at approximately 0.07 Hz throughout the measurement time, corresponding to the cyclic bending frequency. The signal peak value of the crack initiation period is observed to be larger than the propagation period, but the frequency is slower. In addition, another harmonic peak occurs at 0.2 Hz, indicating the longitudinal extension of cracks. Fig. 15c shows that the signal frequency increases significantly with the extension of cracks. Furthermore, when a rupture occurs, the frequency and amplitude of the signal increased considerably. These results demonstrated that the CFRP/KNN–EP sensor can characterize crack growth paths and fracture for damage detection.

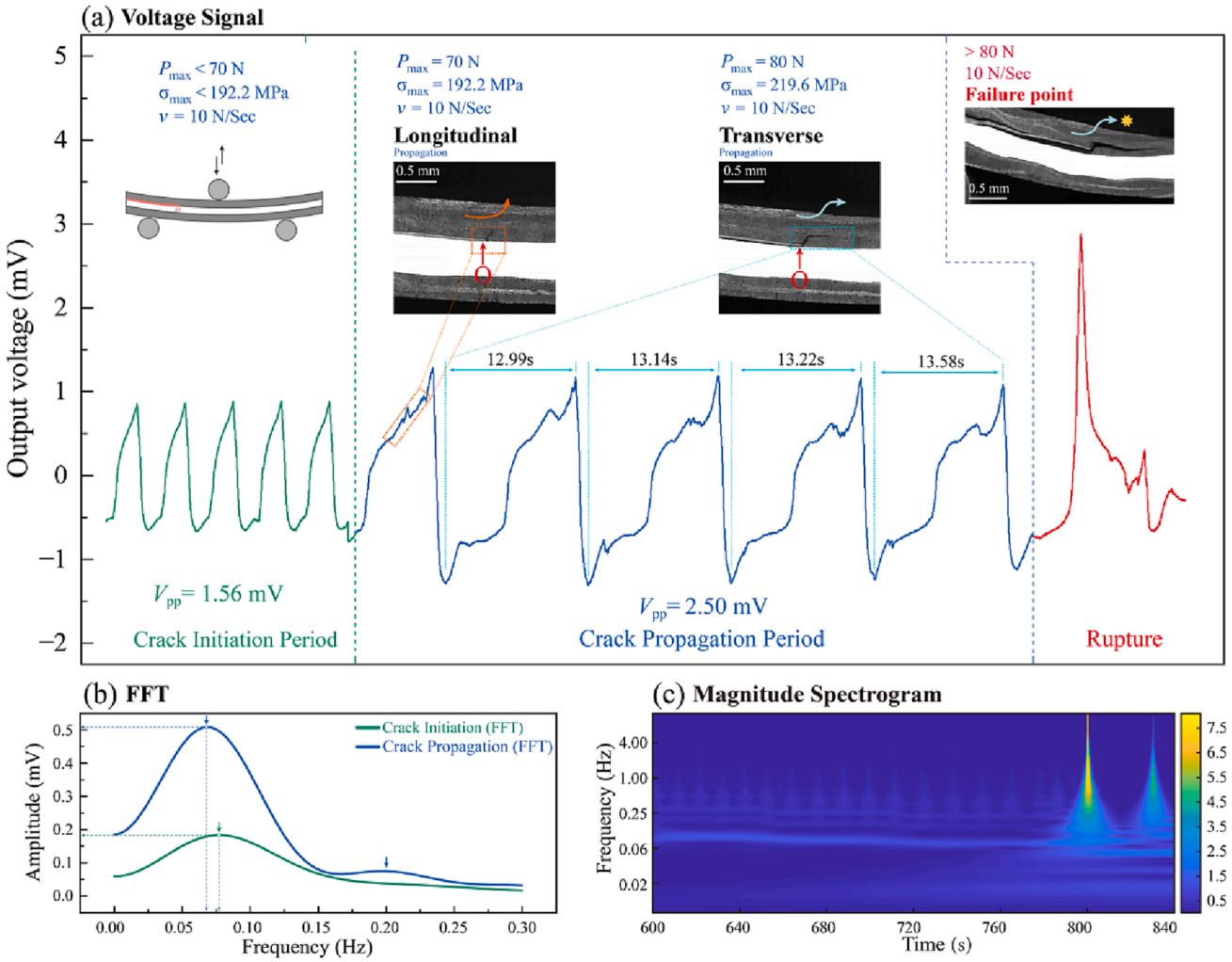

Fig. 15. Case 3: using ENF CFRP/KNN–EP for damage detection in a cyclic 3-point bending test. (a) Voltage signal, the inset is cross-sectional observation. (b) FFT spectrum analysis, and (c) magnitude spectrogram (unit: mV).

Table B.1
The properties of the CFRP/KNN–EP components used in the calculation.

Parameters	E_{22}^{cf}(GPa)	E_{22}^{cf} (GPa)	E_{11}^{p} (GPa)	E_{22}^{p} (GPa)	v_{12}^{cf}	v_{21}^{cf}	v_{12}^{p}	v_{21}^{p}
Measured value	54.9	54.9	6.2	6.2	0.3	0.3	0.35	0.35

4. Conclusion

A KNN-EP plate was developed and combined with advanced CFRP electrodes to obtain a composite with enhanced mechanical and piezoelectric properties. Two manufacturing methods of CFRP/KNN–EP composites were proposed and compared to optimize the process. The poling process followed by the CFRP electrode molding can improve the piezoelectrical performance. The KNN–EP plate with a KNN content of 30 vol% exhibits the best piezoelectric and mechanical properties. In addition, the CFRP electrode significantly increases the maximum bending stress of the composite; it increases the output voltage amplitude to 7.25 mV, which is 600 % higher than that of the original KNN–EP plate (1.03 mV). This indicates that CFRP/KNN–EP has the potential to collect environmental energy. Alternatively, the results showed that crack growth and interlaminar damage behaviors correspond to the output voltage signals, including peak value, frequency, and split peaks, which prove the crack propagation and indicate the imminent rupture. Overall, this work proposed a new strategy for combining carbon fiber reinforcement and piezoelectric polymers to obtain excellent mechanical properties and high sensing sensitivity for damage detection.

CRediT authorship contribution statement

Yaonan Yu: Formal analysis, Investigation, Writing – original draft, Resources, Visualization. **Yu Shi:** Conceptualization, Methodology, Data curation, Validation. **Hiroki Kurita:** Validation, Project administration. **Yu Jia:** Writing – review & editing. **Zhenjin Wang:** Writing – review & editing. **Fumio Narita:** Writing – review & editing, Supervision, Funding acquisition.

Declaration of Competing Interest

The authors declare that they have no known competing financial interests or personal relationships that could have appeared to influence the work reported in this paper.

Data availability

Data will be made available on request.

Acknowledgments

The authors greatly acknowledge the support of this work by the Japan Society for the Promotion of Science, Grant-in-Aid for Scientific Research (A) under Grant No. 22H00183 and Core-to-Core Program under Grant No. JPJSCCA20200005.

Appendix A

Constitutive equations of the piezoelectric ceramics, belonging to the orthorhombic crystal classmm2, poled in the x_3-direction can be written as follows:

$$\begin{Bmatrix} \varepsilon_{11} \\ \varepsilon_{22} \\ \varepsilon_{33} \\ 2\varepsilon_{23} \\ 2\varepsilon_{31} \\ 2\varepsilon_{12} \end{Bmatrix} = \begin{bmatrix} s_{11}^{E} & s_{12}^{E} & s_{13}^{E} & 0 & 0 & 0 \\ s_{12}^{E} & s_{22}^{E} & s_{13}^{E} & 0 & 0 & 0 \\ s_{13}^{E} & s_{13}^{E} & s_{33}^{E} & 0 & 0 & 0 \\ 0 & 0 & 0 & s_{44}^{E} & 0 & 0 \\ 0 & 0 & 0 & 0 & s_{44}^{E} & 0 \\ 0 & 0 & 0 & 0 & 0 & s_{66}^{E} \end{bmatrix} \begin{Bmatrix} \sigma_{11} \\ \sigma_{22} \\ \sigma_{33} \\ \sigma_{23} \\ \sigma_{31} \\ \sigma_{12} \end{Bmatrix} + \begin{bmatrix} 0 & 0 & d_{31} \\ 0 & 0 & d_{32} \\ 0 & 0 & d_{33} \\ 0 & d_{24} & 0 \\ d_{15} & 0 & 0 \\ 0 & 0 & 0 \end{bmatrix} \begin{Bmatrix} E_1 \\ E_2 \\ E_3 \end{Bmatrix} \tag{A.1}$$

$$\begin{Bmatrix} D_1 \\ D_2 \\ D_3 \end{Bmatrix} = \begin{bmatrix} 0 & 0 & 0 & 0 & d_{15} & 0 \\ 0 & 0 & 0 & d_{24} & 0 & 0 \\ d_{31} & d_{32} & d_{33} & 0 & 0 & 0 \end{bmatrix} \begin{Bmatrix} \sigma_{11} \\ \sigma_{22} \\ \sigma_{33} \\ \sigma_{23} \\ \sigma_{31} \\ \sigma_{12} \end{Bmatrix} + \begin{bmatrix} \epsilon_{11}^{T} & 0 & 0 \\ 0 & \epsilon_{22}^{T} & 0 \\ 0 & 0 & \epsilon_{33}^{T} \end{bmatrix} \begin{Bmatrix} E_1 \\ E_2 \\ E_3 \end{Bmatrix} \tag{A.2}$$

where ε_{ij} and σ_{ij} are the components of strain and stress tenors, D_i and E_i are the components of electric displacement and electric field intensity vectors, s_{ij}^{E}, d_{ij}, and ϵ_{ij}^{T} are the elastic compliance at constant electric field, piezoelectric coefficient, and permittivity at constant stress, respectively.

For piezoelectric layer in the state of plane stress, we have

$$\sigma_{33} = 0, \sigma_{23} = 0, \sigma_{31} = 0 \tag{A.3}$$

leaving the constitutive equations (A.1) and (A.2) as

$$\begin{Bmatrix} \sigma_{11} \\ \sigma_{22} \\ \sigma_{12} \end{Bmatrix} = \begin{bmatrix} Q_{11} & Q_{12} & 0 \\ Q_{12} & Q_{22} & 0 \\ 0 & 0 & Q_{66} \end{bmatrix} \begin{Bmatrix} \varepsilon_{11} \\ \varepsilon_{22} \\ 2\varepsilon_{12} \end{Bmatrix} - \begin{bmatrix} 0 & 0 & e_{31}^{'} \\ 0 & 0 & e_{32}^{'} \\ 0 & 0 & 0 \end{bmatrix} \begin{Bmatrix} E_1 \\ E_2 \\ E_3 \end{Bmatrix} \tag{A.4}$$

$$\begin{Bmatrix} D_1 \\ D_2 \\ D_3 \end{Bmatrix} = \begin{bmatrix} 0 & 0 & 0 \\ 0 & 0 & 0 \\ e_{31}^{'} & e_{32}^{'} & 0 \end{bmatrix} \begin{Bmatrix} \varepsilon_{11} \\ \varepsilon_{22} \\ 2\varepsilon_{12} \end{Bmatrix} + \begin{bmatrix} \epsilon_{11}^{T} & 0 & 0 \\ 0 & \epsilon_{22}^{T} & 0 \\ 0 & 0 & \epsilon_{33}^{'T} \end{bmatrix} \begin{Bmatrix} E_1 \\ E_2 \\ E_3 \end{Bmatrix} \tag{A.5}$$

where

$$Q_{11} = \frac{s_{22}^{E}}{s_{11}^{E}s_{22}^{E} - (s_{12}^{E})^2} = \frac{E_{11}^{p}}{1 - \nu_{12}^{p}\nu_{21}^{p}},$$

$$Q_{22} = \frac{s_{11}^{E}}{s_{11}^{E}s_{22}^{E} - (s_{12}^{E})^2} = \frac{E_{22}^{p}}{1 - \nu_{12}^{p}\nu_{21}^{p}},$$

$$Q_{12} = \frac{s_{12}^{E}}{s_{11}^{E}s_{22}^{E} - (s_{12}^{E})^2} = \frac{\nu_{12}^{p}E_{22}^{p}}{1 - \nu_{12}^{p}\nu_{21}^{p}} = \frac{\nu_{21}^{p}E_{11}^{p}}{1 - \nu_{12}^{p}\nu_{21}^{p}},$$

$$Q_{66} = \frac{1}{s_{66}^{E}} = G_{12}^{p}$$

$$e_{31}^{'} = d_{31}Q_{11} + d_{32}Q_{12}, e_{32}^{'} = d_{31}Q_{12} + d_{32}Q_{22}$$

$$\epsilon_{33}^{'T} = \epsilon_{33}^{T} - \left(d_{31}^2 Q_{11} + d_{31}^2 Q_{22} + 2d_{31}^2 Q_{12}\right) \tag{A.6}$$

In Eq. (A.6), E_{11}^p, E_{22}^p are Young's moduli, ν_{12}^p, ν_{21}^p are Poisson's ratio, and G_{12}^p is the shear modulus. The superscript p denotes piezoelectric layer.

Appendix B

The constitutive equations for a piezoelectric layer 2 become

$$\begin{Bmatrix} \sigma_{xx} \\ \sigma_{yy} \\ \sigma_{xy} \end{Bmatrix}_2 = \begin{bmatrix} \bar{Q}_{11} & \bar{Q}_{12} & 0 \\ \bar{Q}_{12} & \bar{Q}_{22} & 0 \\ 0 & 0 & \bar{Q}_{66} \end{bmatrix}_2 \begin{Bmatrix} \varepsilon_{xx} \\ \varepsilon_{yy} \\ 2\varepsilon_{xy} \end{Bmatrix}_2 - \begin{bmatrix} 0 & 0 & \bar{e}_{31} \\ 0 & 0 & \bar{e}_{32} \\ 0 & 0 & 0 \end{bmatrix}_2 \begin{Bmatrix} E_x \\ E_y \\ E_z \end{Bmatrix}_2 \tag{B.1}$$

$$\begin{Bmatrix} D_x \\ D_y \\ D_z \end{Bmatrix}_2 = \begin{bmatrix} 0 & 0 & 0 \\ 0 & 0 & 0 \\ \bar{e}_{31} & \bar{e}_{32} & 0 \end{bmatrix}_2 \begin{Bmatrix} \varepsilon_{xx} \\ \varepsilon_{yy} \\ 2\varepsilon_{xy} \end{Bmatrix}_2 + \begin{bmatrix} \bar{\epsilon}_{11} & 0 & 0 \\ 0 & \bar{\epsilon}_{22} & 0 \\ 0 & 0 & \bar{\epsilon}_{33} \end{bmatrix}_2 \begin{Bmatrix} E_x \\ E_y \\ E_z \end{Bmatrix}_2 \tag{B.2}$$

where

$$(\bar{Q}_{11})_2 = Q_{11}$$

$$(\bar{Q}_{12})_2 = Q_{12}$$

$$(\bar{Q}_{22})_2 = Q_{22}$$

$$(\bar{Q}_{66})_2 = Q_{66}$$

$$(\bar{e}_{31})_2 = e_{31}^{'}, (\bar{e}_{32})_2 = e_{32}^{'}$$

$$(\bar{\epsilon}_{11})_2 = \epsilon_{11}^{T}, (\bar{\epsilon}_{22})_2 = \epsilon_{22}^{T}$$

$$(\bar{\epsilon}_{33})_2 = \epsilon_{33}^{'T} \tag{B.3}$$

For an open-circuit condition, the electrical displacement is

$$(D_z)_2 = 0 \tag{B.4}$$

So, from Eq.(B.2), the electric field within the piezoelectric layer due to the mechanical loading is obtained as follows:

$$(E_z)_2 = -\frac{(\bar{e}_{31})_2(\varepsilon_{xx})_2 + (\bar{e}_{32})_2(\varepsilon_{yy})_2}{(\bar{\epsilon}_{33})_2} \tag{B.5}$$

Substituting Eq. (B. 5) into Eq. (B. 1) results in the following:

$$(\sigma_{xx})_2 = \left[(\bar{Q}_{11})_2 + \frac{(\bar{e}_{31})_2^{\,2}}{(\epsilon_{33})_2}\right](\varepsilon_{xx})_2 + \left[(\bar{Q}_{12})_2 + \frac{(\bar{e}_{31})_2(\bar{e}_{32})_2}{(\epsilon_{33})_2}\right](\varepsilon_{yy})_2$$

$$(\sigma_{yy})_2 = \left[(\bar{Q}_{12})_2 + \frac{(\bar{e}_{31})_2(\bar{e}_{32})_2}{(\epsilon_{33})_2}\right](\varepsilon_{xx})_2 + \left[(\bar{Q}_{22})_2 + \frac{(\bar{e}_{32})_2^{\,2}}{(\epsilon_{33})_2}\right](\varepsilon_{yy})_2$$

$$(\sigma_{xy})_2 = 2(\bar{Q}_{66})_2(\varepsilon_{xy})_2 \tag{B.6}$$

Hence, the reduced stiffness constants of piezoelectric layer under open-circuit condition can be obtained as follows:

$$\bar{Q}_{11}^p = (\bar{Q}_{11})_2 + \frac{(\bar{e}_{31})_2^{\,2}}{(\bar{\epsilon}_{33})_2}$$

$$\bar{Q}_{22}^p = (\bar{Q}_{22})_2 + \frac{(\bar{e}_{32})_2^{\,2}}{(\bar{\epsilon}_{33})_2}$$

$$\bar{Q}_{12}^p = (\bar{Q}_{12})_2 + \frac{(\bar{e}_{31})_2(\bar{e}_{32})_2}{(\bar{\epsilon}_{33})_2} \tag{B.7}$$

The constitutive equations for a CFRP layer $k = 1, 3$ become

$$\begin{Bmatrix}\sigma_{xx}\\ \sigma_{yy}\\ \sigma_{xy}\end{Bmatrix}_k = \begin{bmatrix}\bar{Q}_{11}^{cf} & \bar{Q}_{12}^{cf} & 0\\ \bar{Q}_{12}^{cf} & \bar{Q}_{22}^{cf} & 0\\ 0 & 0 & \bar{Q}_{66}^{cf}\end{bmatrix}_k \begin{Bmatrix}\varepsilon_{xx}\\ \varepsilon_{yy}\\ 2\varepsilon_{xy}\end{Bmatrix} (k = 1, 3) \tag{B.8}$$

where

$$(\bar{Q}_{11}^{cf})_k = \frac{E_{11}^{cf}}{1 - v_{12}^{cf} v_{21}^{cf}}$$

$$(\bar{Q}_{22}^{cf})_k = \frac{E_{22}^{cf}}{1 - v_{12}^{cf} v_{21}^{cf}}$$

$$(\bar{Q}_{12}^{cf})_k = \frac{v_{21}^{cf} E_{11}^{cf}}{1 - v_{12}^{cf} v_{21}^{cf}} = \frac{v_{12}^{cf} E_{22}^{cf}}{1 - v_{12}^{cf} v_{21}^{cf}} \tag{B.9}$$

where the superscript *cf* represents the CFRP layer.

The bending stiffness are

$$D_{11}^{*} = \frac{D_{11} D_{22} - D_{12}^{2}}{D_{22}}$$

$$D_{22}^{*} = \frac{D_{11} D_{22} - D_{12}^{2}}{D_{11}}$$

$$D_{12}^{*} = \frac{D_{11} D_{22} - D_{12}^{2}}{-D_{12}} \tag{B.10}$$

where

$$D_{ij} = b\left\{ \int_{z_0}^{z_1} (Q_{ij}^{cf})_1 z^2 dz + \int_{z_1}^{z_2} (Q_{ij}^{p})_2 z^2 dz + \int_{z_2}^{z_3} (Q_{ij}^{cf})_3 z^2 dz \right\} \tag{B.11}$$

The measured values of Young's moduli (E_{11}^{cf}, E_{22}^{cf}, E_{11}^{p}, E_{22}^{p}) and Poisson's ratios (v_{12}^{cf}, v_{21}^{cf}, v_{12}^{p}, v_{21}^{p}) are listed in Table B.1.

References

[1] Shi J, Bao L, Kobayashi R, Kato J, Kemmochi K. Reusing recycled fibers in high-value fiber-reinforced polymer composites: Improving bending strength by surface cleaning. Compos Sci Technol 2012;72:1298–303. https://doi.org/10.1016/j.compscitech.2012.05.003.

[2] Alam P, Mamalis D, Robert C, Floreani C, Ó Brádaigh CM. The fatigue of carbon fibre reinforced plastics - a review. Compos B Eng 2019;166:555–79. https://doi.org/10.1016/j.compositesb.2019.02.016.

[3] Kaushik V, Siddgonde N, Narita F, Ghosh A. Mode-I fracture control of unidirectional laminated composites using MFC actuators. J Intell Mater Syst Struct 2022;33:2440–53. https://doi.org/10.1177/1045389X221088032.

[4] Meier U. Strengthening of structures using carbon fibre/epoxy composites. Constr Build Mater 1995;9:341–351.. https://doi.org/10.1016/0950-0618(95)00071-2.

[5] Jiang F, Ding Y, Song Y, Geng F, Wang Z. CFRP strengthening of fatigue cracks at U-rib to diaphragm welds in orthotropic steel bridge decks: experimental study, optimization, and decision-making. Structures 2022;43:1216–29. https://doi.org/10.1016/j.istruc.2022.07.039.

[6] Li RW, Zhang N, Wu H. Effectiveness of CFRP shear-strengthening on vehicular impact resistance of double-column RC bridge pier. Eng Struct 2022;266:114604. https://doi.org/10.1016/j.engstruct.2022.114604.

[7] Scuro C, Lamonaca F, Porzio S, Milani G, Olivito RS. Internet of things (IoT) for masonry structural health monitoring (SHM): overview and examples of innovative systems. Constr Build Mater 2021;290:123092. https://doi.org/10.1016/j.conbuildmat.2021.123092.

[8] Karimian SF, Modarres M. Acoustic emission signal clustering in CFRP laminates using a new feature set based on waveform analysis and information entropy analysis. Compos Struct 2021;268:113987. https://doi.org/10.1016/j.compstruct.2021.113987.

[9] Seychal G, Ramasso E, Le Moal P, Bourbon G, Gabrion X, Placet V. Towards in-situ acoustic emission-based health monitoring in bio-based composites structures: does embedment of sensors affect the mechanical behaviour of flax/epoxy laminates? Compos B Eng 2022;236:109787. https://doi.org/10.1016/j.compositesb.2022.109787.

[10] Wang Y, Chen G, Wang Y, Han B, Wan B, Hao Q, et al. Tensile strain and damage self-sensing of flax FRP laminates using carbon nanofiber conductive network coupled with acoustic emission. Compos Struct 2022;290:115549. https://doi.org/10.1016/j.compstruct.2022.115549.

[11] Feng D, Feng MQ. Computer vision for SHM of civil infrastructure: From dynamic response measurement to damage detection – a review. Eng Struct 2018;156:105–17. https://doi.org/10.1016/j.engstruct.2017.11.018.

[12] Shao Y, Li L, Li J, An S, Hao H. Computer vision based target-free 3D vibration displacement measurement of structures. Eng Struct 2021;246:113040. https://doi.org/10.1016/j.engstruct.2021.113040.

[13] Avci O, Abdeljaber O. Self-organizing maps for structural damage detection: a novel unsupervised vibration-based algorithm. J Perform Constr Facil 2016:30. https://doi.org/10.1061/(ASCE)CF.1943-5509.0000801.

[14] Alsaadi A, Meredith J, Swait T, Curiel-Sosa JL, Jia Y, Hayes S. Structural health monitoring for woven fabric CFRP laminates. Compos B Eng 2019;174:107048. https://doi.org/10.1016/j.compositesb.2019.107048.

[15] Narita F, Fox M. A review on piezoelectric, magnetostrictive, and magnetoelectric materials and device technologies for energy harvesting applications. Adv Eng Mater 2018;20:1700743. https://doi.org/10.1002/adem.201700743.

[16] Rana MM, Khan AA, Zhu W, Al Fattah MFA, Kokilathasan S, Rassel S, et al. Enhanced piezoelectricity in lead-free halide perovskite nanocomposite for self-powered wireless electronics. Nano Energy 2022;101:107631. https://doi.org/10.1016/j.nanoen.2022.107631.

[17] Takaishi K, Kubota Y, Kurita H, Wang Z, Narita F. Fabrication and electromechanical characterization of mullite ceramic fiber/thermoplastic polymer piezoelectric composites. J Am Ceram Soc 2022;105:308–16. https://doi.org/10.1111/jace.18047.

[18] Narita F, Wang Z, Kurita H, Li Z, Shi Y, Jia Y, et al. A review of piezoelectric and magnetostrictive biosensor materials for detection of COVID-19 and other viruses. Adv Mater 2021;33:2005448. https://doi.org/10.1002/adma.202005448.

[19] Wang Y, Yu Y, Wei X, Narita F. Self-powered wearable piezoelectric monitoring of human motion and physiological signals for the postpandemic era: a review. Adv Mater Technol 2022;7:2200318. https://doi.org/10.1002/admt.202200318.

[20] Hwang MY, Kang LH. Characteristics and fabrication of piezoelectric GFRP using smart resin prepreg for detecting impact signals. Compos Sci Technol 2018;167:224–33. https://doi.org/10.1016/j.compscitech.2018.08.002.

[21] Wang Q, Tian Y, Duongthipthewa A, Zhang J, Liu M, Su Z, et al. An embedded non-intrusive graphene/epoxy broadband nanocomposite sensor co-cured with GFRP for in situ structural health monitoring. Compos Sci Technol 2023;236:109995. https://doi.org/10.1016/j.compscitech.2023.109995.

[22] Malinowski P, Wandowski T, Ostachowicz W. The use of electromechanical impedance conductance signatures for detection of weak adhesive bonds of carbon

fibre–reinforced polymer. Struct Health Monit 2015;14:332–44. https://doi.org/10.1177/1475921715586625.
[23] Yuan L, Fan W, Yang X, Ge S, Xia C, Foong SY, et al. Piezoelectric PAN/BaTiO3 nanofiber membranes sensor for structural health monitoring of real-time damage detection in composite. Compos Commun 2021;25:100680. https://doi.org/10.1016/j.coco.2021.100680.
[24] Gino ME, Selleri G, Cocchi D, Brugo TM, Testoni N, De Marchi L, et al. On the design of a piezoelectric self-sensing smart composite laminate. Mater Des 2022;219:110783. https://doi.org/10.1016/j.matdes.2022.110783.
[25] Wang Z, Kurita H, Nagaoka H, Narita F. Potassium sodium niobate lead-free piezoelectric nanocomposite generators based on carbon-fiber-reinforced polymer electrodes for energy-harvesting structures. Compos Sci Technol 2020;199:108331. https://doi.org/10.1016/j.compscitech.2020.108331.
[26] Chen B, Jia Y, Narita F, Wang C, Shi Y. Multifunctional cellular sandwich structures with optimised core topologies for improved mechanical properties and energy harvesting performance. Compos B Eng 2022;238:109899. https://doi.org/10.1016/j.compositesb.2022.109899.
[27] Yu Y, Narita F. Evaluation of electromechanical properties and conversion efficiency of piezoelectric nanocomposites with carbon-fiber-reinforced polymer electrodes for stress sensing and energy harvesting. Polymers (Basel) 2021;13:3184. https://doi.org/10.3390/polym13183184.
[28] Wang Z, Narita F. Corona poling conditions for barium titanate/epoxy composites and their unsteady wind energy harvesting potential. Adv Eng Mater 2019;21:1900169. https://doi.org/10.1002/adem.201900169.
[29] Guo W, Long Y, Bai Z, Wang X, Liu H, Guo Z, et al. Variable stiffness triboelectric nano-generator to harvest high-speed railway bridge's vibration energy. Energy Convers Manag 2022;268:115969. https://doi.org/10.1016/j.enconman.2022.115969.
[30] Maruyama K, Kawakami Y, Mori K, Kurita H, Shi Y, Jia Y, et al. Electromechanical characterization and kinetic energy harvesting of piezoelectric nanocomposites reinforced with glass fibers. Compos Sci Technol 2022;223:109408. https://doi.org/10.1016/j.compscitech.2022.109408.
[31] Ponraj B, Bhimireddi R, Varma KBR. Effect of Nano- and micron-sized K0.5Na0.5NbO3 fillers on the dielectric and piezoelectric properties of PVDF composites. J Adv Ceram 2016;5:308–20. https://doi.org/10.1007/s40145-016-0204-2.
[32] Du H, Zhou W, Luo F, Zhu D, Qu S, Pei Z. An approach to further improve piezoelectric properties of $(K_{0.5}Na_{0.5})NbO_3$-based lead-free ceramics. Appl Phys Lett 2007;91:202907. https://doi.org/10.1063/1.2815750.
[33] Rahman A, Jiang M, Rao G, Lee S, Kim MH, Habib M, et al. Improved ferroelectric, piezoelectric, and dielectric properties in pure KNN translucent ceramics by optimizing the normal sintering method. Ceram Int 2022;48:20251–9. https://doi.org/10.1016/j.ceramint.2022.03.305.
[34] Zheng T, Wu J, Xiao D, Zhu J. Recent development in lead-free perovskite piezoelectric bulk materials. Prog Mater Sci 2018;98:552–624. https://doi.org/10.1016/j.pmatsci.2018.06.002.